Nanostructure Evolution Mechanisms During Slow Load-Cycling of Oriented HDPE/PA Microfibrillar Blends as a Function of Composition

Ahmad Zeinolebadi[1], Norbert Stribeck[1*], Morteza Ganjaee-Sari[2], Nadya Dencheva[3], Zlatan Denchev[3], Stephan Botta[4]

[1]Department of Chemistry, Institute of Technical and Macromolecular Chemistry, University of Hamburg, Bundesstr. 45, 20146 Hamburg, Germany; Fax: (+49) 40 42838 6008; E-mail: norbert@stribeck.de
[2]Department of Polymer Engineering and Color Technology, Amirkabir University of Technology, 424 Hafez Ave, Tehran, Iran, P.O. 15875-4413
[3]i3N – IPC, University of Minho, Guimarães 4800-058, Portugal
[4]HASYLAB at DESY, Notkestr. 85, D-22603 Hamburg, Germany

Oriented precursors of microfibrillar reinforced composites (MFC) are studied during strain-controlled slow load-cycling by small-angle X-ray scattering (SAXS). The samples contain high-density polyethylene (HDPE) and polyamide 6 (PA6) or polyamide 12 (PA12). Some samples contain 10 wt.-% compatibilizer. SAXS probes the response of the nanofibrillar semi-crystalline entities from the HDPE microfibrils. In the PA6-containing blends strongly retarded nanostrain response is detected. It is suppressed by compatibilization. Compatibilization induces nanostrain heterogenization in the experiment. Stress fatigue is lower in the PA12-blends, but hardly decreased by compatibilizer. Selective migration of compatibilizer into a disordered semi-crystalline fraction of the HDPE matrix explains the findings. The semi-crystalline HDPE entities in PA6-blends appear more disordered than in PA12-blends. An analysis of the HDPE-nanostructure evolution during cycling reveals epitaxial strain crystallization and other mechanisms. Respective evolution cycles are sketched. Uncompatibilized PA6-blends cycled about high pre-strain show plastic flow but nanoscopic shrinkage in the semi-crystalline stacks that may be explained by extinction of frozen-in tensions around the stacks.

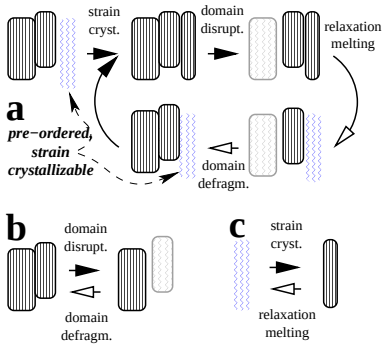

1 Introduction

The combination of several polymers in a polymer-polymer composite promises both improved properties during service and low ash content after incineration[1–3]. Improved mechanical properties are required to replace metal by lightweight parts in automobiles. Low ash content is a European legislative request [4–6] that must be met in the future. Microfibrillar reinforced composites (MFC) are polymer-polymer composites made from thermodynamically immiscible polymers in which both the isotropic matrix and the fibrous anisotropic reinforcements are formed *in-situ* during processing[7,8]. The fabrication of MFCs begins with the melt–blending followed by cold–drawing. In so doing, the domains of the semi-crystalline blend components are transformed into microfibrils, thus forming the so-called oriented precursor blends. Finally, these precursors are molded (most frequently by compression molding) at temperatures below the melting of the fibril-forming component and above that of the matrix-forming component. Hence, only the matrix polymer is isotropized, whereas the microfibrils of the reinforcements maintain their shape and orientation.

In many practical applications that MFCs are designed for, the materials are subjected to cyclic (dynamic) load. Hence, resistance[9] to dynamic loads (i.e. low fatigue[10–12]) is required. There is abundant literature on the relation between the nanostructure of polymeric materials and their behavior under mechanical loading[13]. For such studies an advantageous experiment is the monitoring of mechanical tests by X-ray scattering methods[14,15], because both mechanical and structural data are recorded at the same time. Nevertheless, papers in which structure variations are studied simultaneously during fatigue tests are still rare[16–18]. Fortunately, recent progress at synchrotron radiation sources facilitates to monitor at least slow dynamic tests with frequencies ranging between 10^{-3} Hz and 10^{-1} Hz, because now low-noise anisotropic scattering patterns of polymers can be recorded within 20 s down to 1 s. In practice though, typical cycling frequencies of fatigue tests are much higher (1–1000 Hz). Nevertheless, some insight about fatigue mech-

anisms of polymers may be gained even from the study of structure variation during slow dynamic experiments.

In recent studies, synchrotron wide- and small angle X-ray scattering (WAXS, SAXS) and electron microscopy methods have been used to investigate the nanostructure variations in MFCs made from high-density polyethylene (HDPE) and two different polyamides (PA12 and PA6). The studies of HDPE/PA12[19] and HDPE/PA6 MFCs[20] have been carried out at various temperatures without application of strain. It has been shown that a direct relation exists between the mechanical properties of the respective MFCs and their nanostructural parameters, e.g., the thickness of an oriented HDPE transcrystalline layer on the oriented PA fibrils. In order to retrieve this result the isotropic fraction of WAXS and SAXS has been removed[19,21] from the patterns in order to emphasize the scattering effect of the oriented fibril reinforcements. In the present study we examine the evolution of the nanostructure in MFC precursors, i.e. in materials that have not yet been subjected to the final annealing step which eliminates the orientation of the matrix.

2 Experimental

2.1 Materials

MFC precursors are made from high density polyethylene (HDPE) as the major, matrix forming component and from polyamide 6 (PA6) or polyamide 12 (PA12) as the higher melting, reinforcing component. Two samples contain 10 wt.-% of the commercial compatibilizer Yparex®8102. The HDPE is produced by Borealis [PE VS4531®; density 0.94 g/cm^3; melt flow index: 0.6 g / 10 min (2.16 kg, 190 °C); melting point by DSC: 133 °C]. The PA6 is made by Lanxess [Durethan® B30S; density: 1.14 g/cm^3; melt volume flow rate: 110 cm^3/10 min (5 kg, 260 °C, ISO 1133); melting point by DSC: 220 °C]. The PA12 is produced by EMS-GRIVORY [Grilamid® L25; density: 1.01 g/cm^3; melting point by DSC: 178 °C; M_w = 60 kg/mol; M_n = 31 kg/mol]. Yparex®8102 is made by DSM. It is a copolymer of LLDPE and maleic anhydride. Its melt flow index is 2.3 g / 10 min (2.16 kg, 190 °C); melting point by DSC: 125 °C; M_w= 120 kg/mol; M_n= 15 kg/mol. Quantities of granulate have been premixed in the proportions as indicated in Table 1. Each mixture has been melt-blended in a laboratory twin-screw extruder. The extrudate has been cooled to 12 °C and a slight drawing has been applied in the first haul-off unit of the extruder line to stabilize the strand cross-section. Further drawing has been performed in the second haul-off unit after heating the strand in a water bath of 97-98 °C. A third haul-off unit has applied the last drawing causing the diameter of the strand to decrease from 2 mm (at the die outlet) to about 0.6-0.9 mm. Details concerning the principle of the preparation of the HDPE/PA/YP precursors[8] and the design of the extruder line[20] have been published previously.

Table 1: Composition (in wt. %) of oriented blends. In the code P6, P12, H and Y stand for polyamide 6, polyamide 12, HDPE, and the compatibilizer Yparex®8102, respectively

sample code	PA6	PA12	HDPE	Yparex
P6HY(20/80/0)	20	—	80	0
P6HY(20/70/10)	20	—	70	10
P12HY(20/80/0)	—	20	80	0
P12HY(20/70/10)	—	20	70	10

2.2 Mechanical tests

A home-made tensile tester[22] is installed on the X-ray beamline. The sample is mounted in the machine with its draw axis perpendicular to the X-ray beam path. The straining direction is the fiber direction. The tensile machine performs symmetric drawing. Signals from load cell and transducer are recorded during the mechanical tests. After approaching different pre-strains (ca. 5% and ca. 8% strain for low-cycling and high-cycling, respectively) the sample is cycled between two fixed distances of the cross-heads. Thus strain-controlled load-cycling instead of stress-controlled cycling is performed. In the experiments the strain rate, $\dot{\varepsilon}$, is close to $\pm 1.5 \times 10^{-4} s^{-1}$. During the test the sample is monitored by a video camera.

2.3 Small-angle X-ray scattering

SAXS is performed at the synchrotron beamline A2 at HASYLAB, Hamburg, Germany. The wavelength of the X-ray beam is 0.15 nm, and the sample-detector distance is 2542 mm. Scattering patterns are collected by a 2D detector (marccd 165; mar research, Norderstedt, Germany) operated in 1024 × 1024 pixel mode (pixel size: 158.2 × 158.2 μm^2). Thus, for the typical long period of 20 nm a variation of the peak position by one pixel causes a long-period variation of below 1 %. During the deformation experiments, scattering patterns are recorded every 30 s with an exposure time of 23 s. The machine background is recorded for background correction.

3 Data evaluation

3.1 Mechanical parameters

The local macroscopic strain, $\varepsilon(t)$, is determined from the recorded video frames (Figure 1). The method has been published in previous work[23]. A region of interest (ROI) is defined close to the beam position. The "correlation function" of the fiducial-mark structure inside the ROI is computed. The required precision of peak-position determination

is reached by fitting the "long-period peak" of the correlation function by a quadratic parabola. Assuming constant volume during mechanical loading, the actual cross-section, $A(t)$, is calculated from

$$A(t) = \frac{A(0)}{\varepsilon(t)+1}. \quad (1)$$

Here $A(0)$ is the initial cross section of the sample. Let $F(t)$ the actual force recorded by the tensile machine. Then the true stress, σ, is

$$\sigma(t) = \frac{F(t)}{A(t)}. \quad (2)$$

The true stress averaged over one cycle, $\bar{\sigma}$, has also been calculated in order to assess fatigue in the load-cycling test.

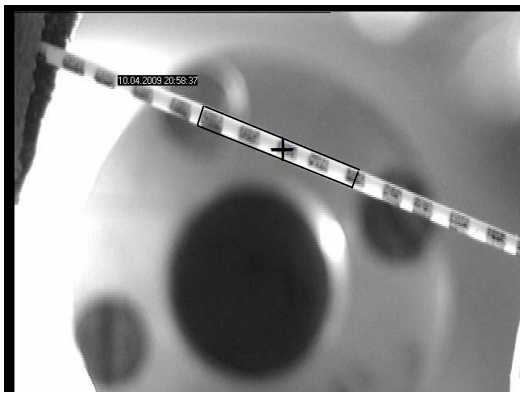

Figure 1: A video frame taken from a series that is used to determine the local macroscopic strain ε. The fiber carries fiducial marks. The cross indicates the position of the center of the primary beam. The box is the ROI (region of interest). From the image inside the ROI the correlation function $\gamma(l)$ is computed. A peak fit of $\gamma(l)$ yields ε, as long as the sample stays taut

3.2 Scattering patterns

The basic data evaluation steps are documented in a text book[24]. The scattering patterns are normalized to the flux of the incident primary beam. Intensity loss due to absorption in the sample is compensated using the measured intensities of the primary beam before and after the sample, respectively. The machine background is subtracted. Pixels in the shades of beam stop and vacuum tube are marked invalid. The fiber pattern is centered and aligned. Part of the invalid regions can be filled from symmetry consideration. The remnant central blind hole is filled applying a stiff parabolic extrapolation[25]. The pattern is projected on the representative fiber plane. Multiplication by s^2 applies the real-space Laplacian. Here s is the modulus of the scattering vector, $\mathbf{s} = (s_{12}, s_3)$, defined by $s = |\mathbf{s}| = (2/\lambda)\sin\theta$. λ is the wavelength of radiation, and 2θ is the scattering angle. The density fluctuation background determined by low-pass filtering is eliminated by subtraction. The resulting interference function, $G(s_{12}, s_3)$, describes the ideal multiphase system. Its 2D Fourier transform is the chord distribution function (CDF)[26], $z(r_{12}, r_3)$. From $G(s_{12}, s_3)$ the scattering intensity $I_{id}(s_{12}, s_3)$ of the ideal multiphase system can be reconstructed. From this pattern the scattering power

$$Q = \iiint I_{id}(s)\, d^3s \quad (3)$$

is computed. Q is already normalized with respect to the irradiated volume, because of the respective normalization of the measured intensity. Because the major fraction of the studied materials is semi-crystalline HDPE, the predominant contribution[24,27–30] to the invariant

$$Q = v(1-v)(\rho_c - \rho_a)^2 + X \quad (4)$$

originates from the two-phase nanostructure of the HDPE with v being its volume crystallinity, and $\rho_c - \rho_a$ the contrast between the electron densities of crystalline and amorphous phase. The additional quantity X is predominantly originating from the embedded microfibrils (PA6 or PA12), and from voids.

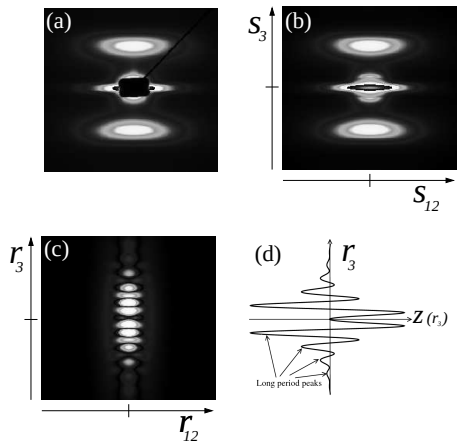

Figure 2: Representative X-ray scattering data of MFC precursors: (**a**) the recorded SAXS pattern. The blind area arises from the shadow of the primary beam-stop (**b**) the corrected fiber diagram $I(s_{12}, s_3)$, (**c**) absolute value of the CDF $|z(r_{12}, r_3)|$, and (d) a one-dimensional slice of the CDF along the meridian $z(0, r_3)$ showing the negative long-period peaks and the positive peaks (above the r_3-axis). Image intensities on logarithmic scale. Displayed regions: $-0.1\,\mathrm{nm}^{-1} < s_{12}, s_3 < 0.1\,\mathrm{nm}^{-1}$, $-100\,\mathrm{nm} < r_{12}, r_3 < 100\,\mathrm{nm}$. The s_3- and r_3-axes match the stretching direction of the sample

Figure 2 shows a representative recorded SAXS pattern, the corrected fiber diagram $I(s_{12}, s_3)$, absolute values of the CDF $|z(r_{12}, r_3)|$ and a slice of the CDF along the meridian, $z(0, r_3)$. The negative peaks in the CDF arise from the correlation between domain surfaces that define the long period and multiples thereof. The peaks on the positive side are related to thicknesses of domains in r_3-direction.

The complex pattern of overlapping peaks in the CDFs reveal a nanostructure that could only be fitted with huge effort. As a result of such a fit the peaks would be separated. Instead, we track the strongest peak in the CDF that is least affected from the tails of the weaker peaks. For the studied materials this peak is the first long-period peak. By fitting the cap of this peak to a bivariate polynomial we retrieve information on the position (L), width (σ_3), and lateral breadth (σ_{12}) of this peak [23]. L is the most probable long period (in r_3-direction) from the distribution of long periods. $e_l = 3\sigma_{12}$ is some measure of the extension of the crystalline domains in lateral direction (i.e. in r_{12}-direction). The kind of measure strongly depends on the shape and the size distributions of the domains. Based on the variations of L, the nanoscopic strain,

$$\varepsilon_n(t) = \frac{L(t)}{L(0)} - 1, \tag{5}$$

is estimated. Similarly, a nanoscopic lateral (in r_{12}-direction) strain,

$$\varepsilon_{n,l}(t) = \frac{e_l(t)}{e_l(0)} - 1, \tag{6}$$

can be defined based on the variations of e_l. These simple parameters are good measures of nanoscopic deformation only as long as the underlying domain-size distributions are deformed affinely[31].

4 Results and discussion

4.1 Micro– and nanostructure

On the micrometer scale the morphology of HDPE/PA oriented precursors has been studied by scanning electron microscope (SEM) in previous work[19,32]. Based on SEM micrographs the average diameter of polyamide microfibrils is 550 ± 100 nm, strongly depending on the HDPE/PA ratio of the cold drawn blend. The length of polyamide microfibrils has been estimated 30-90 µm. Generally, addition of compatibilizer causes a reduction in both diameter and length of polyamide microfibrils[19,32]. Such reduction may be decreased by adding the compatibilizer to a pre-mixed[33,34] blend.

On the nanometer scale the structure of the samples is studied by SAXS. Figure 3 sketches structural features that can be probed by SEM on the micrometer scale and by SAXS on the nanometer scale, respectively. The SAXS of the samples arises mainly from the semi-crystalline structure of the HDPE matrix, as has previously been shown[20]. The reasons are, firstly, that the major component is HDPE. Secondly, polyamide has a low electron density contrast between its crystalline and amorphous regions compared to the corresponding contrast in HDPE.

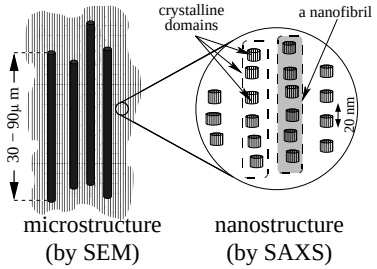

Figure 3: Sketch of typical MFC multi-scale structure at micrometer (left) and nanometer scale (right). Processing direction is vertical. SEM probes the polyamide microfibrils (dark rods) embedded in an oriented HDPE matrix [19,32]. SAXS monitors mainly the semi-crystalline nanostructure of the HDPE matrix. Crystalline domains are frequently arranged in processing direction forming nanofibrils (in the conceptual notion of microfibrils[35]). One nanofibril is highlighted in gray

4.2 Nanostructure of undeformed materials

For the undeformed samples Figure 4 shows the scattering intensities $I(s_{12}, s_3)$ and the absolute values of the corresponding CDFs $z(r_{12}, r_3)$.

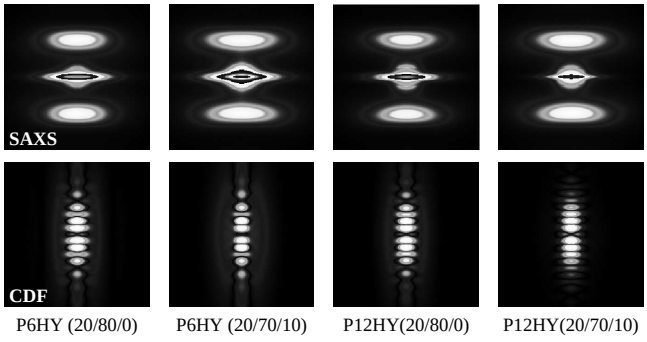

Figure 4: Undeformed samples. SAXS fiber diagrams $I(s_{12}, s_3)$ (top row) and the corresponding CDFs $|z(r_{12}, r_3)|$ (bottom row). Displayed regions: $-0.1\,\mathrm{nm}^{-1} < s_{12}, s_3 < 0.1\,\mathrm{nm}^{-1}$, $-100\,\mathrm{nm} < r_{12}, r_3 < 100\,\mathrm{nm}$. Intensities on logarithmic scale. Fiber axis is vertical

All samples exhibit a layer-line scattering pattern. It is characteristic for a highly oriented structure from slender domains arranged in rows along the fiber axis. The layer lines are not indented or even split into separate peaks. Thus there is only one-dimensional arrangement of domains. This fact is obvious from the CDF data in real space (Figure 4, bottom row). Its peaks and their arrangement directly demonstrate the domains slenderness and their arrangement in fiber direction. The corresponding semi-crystalline morphology is usually called "*microfibrillar*" [35,36]. Instead, here we call it *"nanofibrillar"*, in order to discriminate it from a microfibrillar structure on the micrometer scale (cf. Figure 3). The nanofibrillar SAXS peaks reflected in the CDF only probe

the part of the matrix volume that is filled by semi-crystalline stacks with a minimum arrangement among their constituent domains (ordered stacks). Random placement of irregular domains does not generate discrete SAXS peaks.

The central equatorial streak in the SAXS patterns arises from the envelope of the nanofibrils and from other needle-shaped entities like voids [37,38].

Table 2: Undeformed samples. Essential nanostructure parameters extracted from the CDFs. Long period, L, and an average lateral extension e_l of the HDPE crystalline domains

sample	L [nm]	e_l [nm]
P6HY(20/80/0)	18.6	16.2
P6HY(20/70/10)	18.2	15.1
P12HY(20/80/0)	18.3	16.2
P12HY(20/70/10)	18.9	17.3

Table 2 presents essential nanostructure parameters for the undeformed materials that have been extracted from the strong long-period peak in the CDF. The reported values are averages of measurements from 4 different pieces of the strands. They vary by 5 %. This indicates a slight structure heterogeneity. Table 2 shows that there is little influence of materials composition on the essential nanostructure of the HDPE nanofibrils.

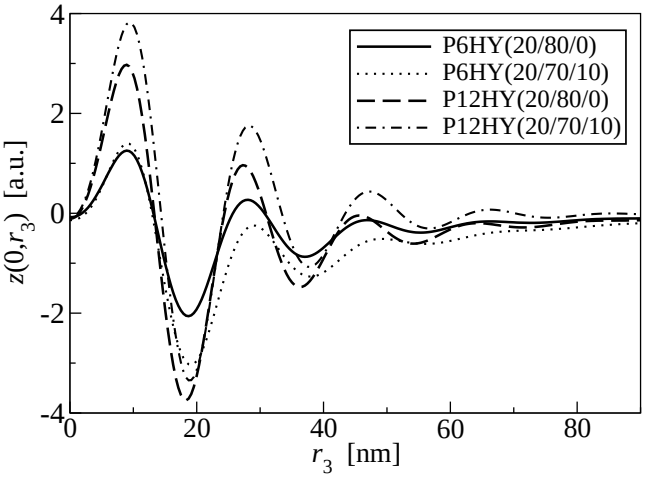

Figure 5: Comparison of $z(0,r_3)$ of undeformed samples. Diffuse merging of the 3rd and 4th negative peaks with the PA6-samples indicates poorer stacking of crystalline domains in its HDPE matrix

In the CDFs from Figure 4, the PA12-reinforced samples show clearer peaks than the PA6-reinforced materials. Figure 5 demonstrates this feature quantitatively by curves cut from the CDFs along its meridional axis. The CDFs of PA12-reinforced materials exhibit four separable long period peaks corresponding to at least five correlated lamellae. However, in the CDFs of the series containing PA6 already the 3rd and 4th long period peak become diffuse and merge. Thus the semi-crystalline HDPE stacks from the blends containing PA6 show more disorder than the respective stacks in blends containing PA12.

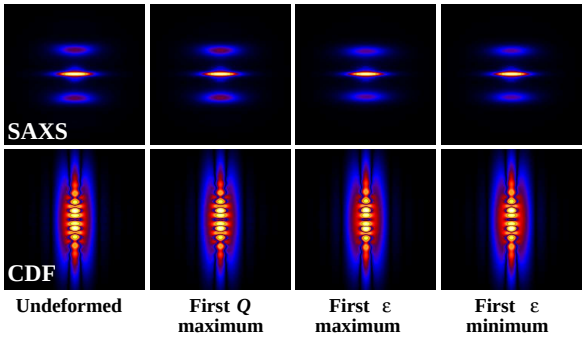

Figure 6: Qualitative similarity of scattering data recorded during load-cycling experiments. Shown are patterns from states of extreme difference during the testing of P6HY(20/80/0) cycled about high pre-strain (8-10%). SAXS fiber diagrams $I(s_{12},s_3)$ (top row) and the corresponding CDFs $|z(r_{12},r_3)|$ (bottom row). Displayed regions: $-0.1\,\mathrm{nm}^{-1} < s_{12},s_3 < 0.1\,\mathrm{nm}^{-1}$, $-75\,\mathrm{nm} < r_{12},r_3 < 75\,\mathrm{nm}$. Intensities on logarithmic scale. Fiber axis is vertical

4.3 General nanostructure evolution in load-cycling tests

During the mechanical tests SAXS patterns have been recorded continuously. Qualitatively these patterns are very similar, as is demonstrated in Figure 6. Hence, it is necessary to extract structural parameters from the patterns with high precision and to analyze their variations. Inspection of the shape-evolution of the CDF peaks shows affine deformation, in contrast to a study of a different class of polymers[31]. Thus the introduced simple nanoscopic structure parameters discussed here are considered to correctly describe the average response of the nanostructure to the applied macroscopic strain.

The evolution of macroscopic-mechanical and of nanoscopic parameters during load-cycling tests is presented in Figure 7 – Figure 10.

4.3.1 Response of stress and nanoscopic strain

In all tests the macroscopic response $\sigma(t)$ to the applied signal $\varepsilon(t)$ is rather simple. The monotonous branches of the saw-tooth function $\varepsilon(t)$ are immediately responded by monotonous branches of $\sigma(t)$. Thus little phase-shift is observed in these low-frequency load-cycling experiments.Compatibilization increases (Figure 8) the stress $\sigma(t)$ for the material reinforced by PA6, as compared to the uncompatibilized sample (Figure 7). At $\varepsilon = 0.06$ the stress increases from 62 MPa to about 80 MPa. The plus with respect to the PA12-reinforced blend is readily explained by the more effective compatibilization in PA6. Due to its different molecular structure, i.e., the lower amounts of CH_2–groups in the repeat units, the chemical bonds between

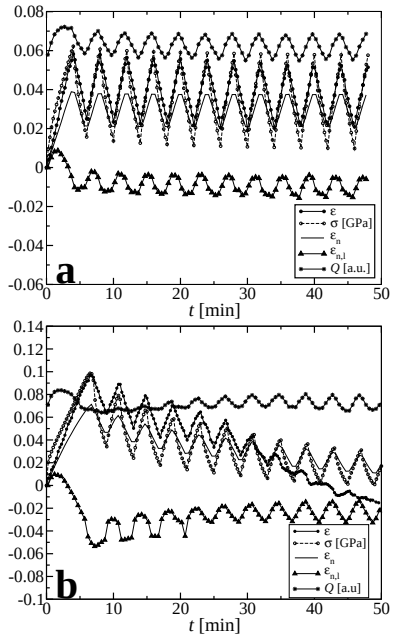

Figure 7: P6HY(20/80/0) load cycling. Mechanical and nanostructure parameters. (**a**) material cycled about low pre-strain (ca. 5%). (**b**) material cycled about high pre-strain (ca. 8%). Mechanical parameters: strain ε and stress σ. Nanostructure parameters: nanostrain ε_n, lateral nanostrain, $\varepsilon_{n,l}$, and scattering power Q. In the high-cycling experiment ε becomes negative

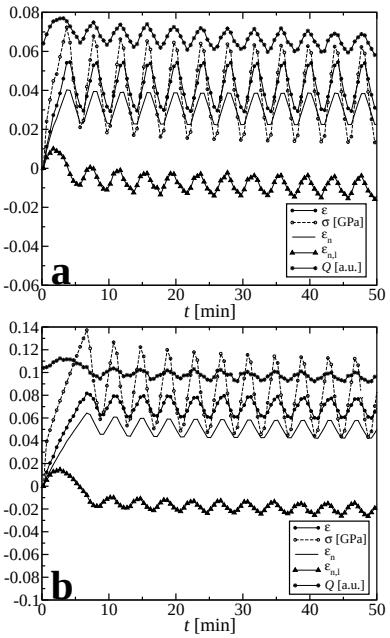

Figure 8: P6HY(20/70/10) load cycling. Mechanical and nanostructure parameters. (**a**) material cycled about low pre-strain. (**b**) material cycled about high pre-strain. Mechanical parameters: strain ε and stress σ. Nanostructure parameters: nanostrain ε_n, lateral nanostrain, $\varepsilon_{n,l}$, and scattering power Q

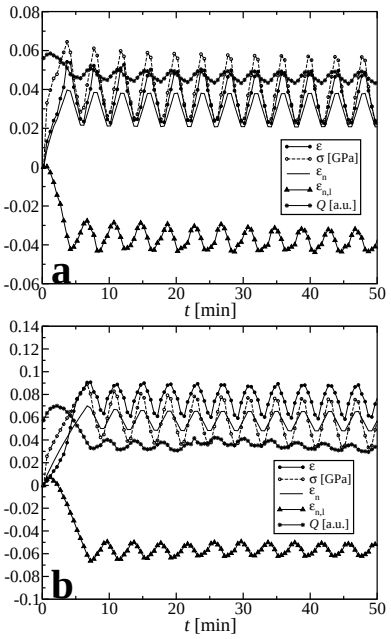

Figure 9: P12HY(20/80/0) load cycling. Mechanical and nanostructure parameters. (**a**) material cycled about low pre-strain. (**b**) material cycled about high pre-strain. Mechanical parameters: strain ε and stress σ. Nanostructure parameters: nanostrain ε_n, lateral nanostrain, $\varepsilon_{n,l}$, and scattering power Q

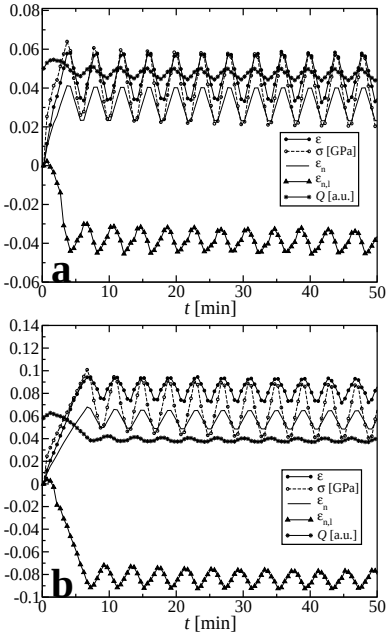

Figure 10: P12HY(20/70/10) load cycling. Mechanical and nanostructure parameters. (**a**) material cycled about low pre-strain. (**b**) material cycled about high pre-strain. Mechanical parameters: strain ε and stress σ. Nanostructure parameters: nanostrain ε_n, lateral nanostrain, $\varepsilon_{n,l}$, and scattering power Q

N-atoms from the PA6 and the anhydride groups from the maleinized HDPE of the compatibilizer are twice as many

as in the case when PA12 reacts with the same compatibilizer[19].

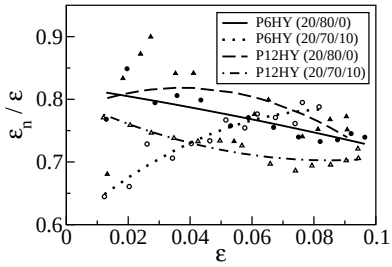

Figure 11: Relative nanoscopic strain, $\varepsilon_n/\varepsilon$, as a function of the local macroscopic strain ε. Data from the first straining branch. The curves are quadratic fits to the data

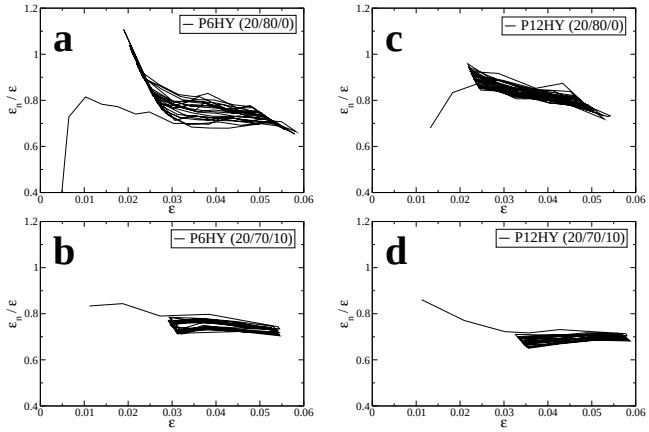

Figure 12: Relative nanoscopic strain, $\varepsilon_n/\varepsilon$, as a function of the local macroscopic strain ε. Data from the complete load-cycling experiments (low pre-strain)

The response of the nanoscopic strain ε_n to the macroscopic strain ε during plain straining is reported in Figure 11. The nanoscopic strain is smaller than the macroscopic strain ($\varepsilon_n < \varepsilon$). ε_n measures only the deformation of the HDPE semi-crystalline stacks. The difference between ε and ε_n indicates a heterogeneous strain distribution in the sample, a common phenomenon in semi-crystalline polymers[39–42]. Humbert et al. [41] have monitored tensile tests of isotropic PE by SAXS. They report relative nanoscopic strains $\varepsilon_n/\varepsilon \approx 0.5$ for $0 < \varepsilon < 0.35$. Our measurements on oriented blends (cf. Figure 11) return values that are closer to the identity $\varepsilon_n = \varepsilon$. For low ε the compatibilized materials show a higher lag of ε_n than the uncompatibilized ones, and the material reinforced by PA12 performs somewhat closer to homogeneous strain than the material that contains PA6. With increasing strain ε, $\varepsilon_n/\varepsilon$ is, in general, further departing from the value $\varepsilon_n/\varepsilon = 1$. This means that in the plain strain experiments the strain heterogeneity is increasing for 3 of the 4 materials. An exception is P6HY(20/70/10) that shows the highest initial strain heterogeneity. Increasing the strain, the strain distribution in this sample becomes more homogeneous, i.e., the trend is inverted as compared to the other samples.

For load-cycling experiments (low pre-strain) Figure 12 presents $\varepsilon_n/\varepsilon$ data. During the test the material P6HY(20/80/0) (Figure 12a) is building up a considerable variation in $\varepsilon_n/\varepsilon$ as a function of ε. As ε is already low, ε_n is still high. Thus here ε_n shows a considerable phase-shift, i.e. a retarded relaxation response. In Figure 12c a similar inclination of the line segments demonstrates that build-up of a retarded relaxation response is also observed with the other uncompatibilized material, P12HY(20/80/0). Nevertheless, here the effect is much weaker. Moreover, the lifting of the inclined line from cycle to cycle towards the level of homogeneity ($\varepsilon_n/\varepsilon = 1$) indicates homogenization of the strain distribution inside the material.

Addition of 10 wt.-% compatibilizer (Figure 12b and Figure 12d) leads to continuous movement of $\varepsilon_n/\varepsilon$ away from the level of homogeneity from cycle to cycle. Thus strain heterogeneity in the compatibilized materials is growing under cyclic load. In summary, the compatibilizer induces strain heterogenization during load cycling, but suppresses the tendency of a retarded nanoscopic structure response.

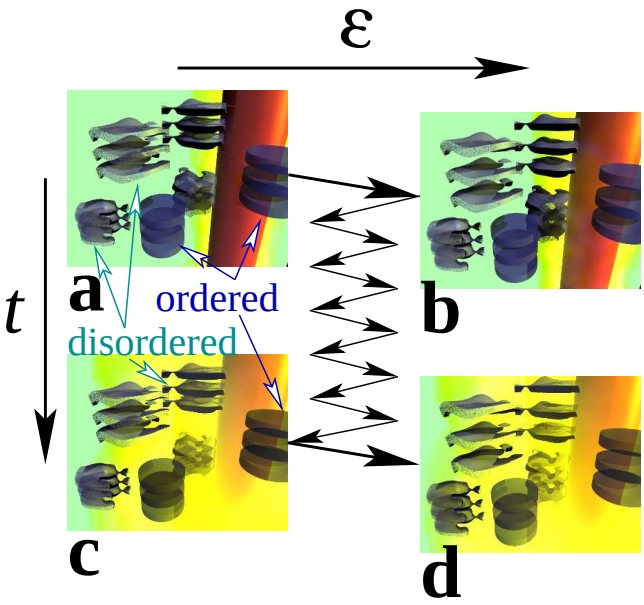

Figure 13: Mechanism of strain heterogenization by selective migration of compatibilizer (yellow haze) away from the PA microfibrils (long red rod) into the disordered fraction (distorted crystalline layers) of the HDPE matrix avoiding the ordered stacks (ideal crystalline discs). The course of macroscopic strain ε in time t is indicated by arrows. (a) Nanostructure before application of load. (b) Expanded nanostructure at the first maximum of strain. (c) Retracted nanostructure after several cycles at a minimum strain. (d) Reaching the upper dead center after several cycles the distance between the distorted layers is longer than at the first maximum (b) because of a plasticizing effect of the compatibilizer

Increasing strain heterogeneity in the HDPE phase dur-

ing the cyclic loading of only the compatibilized materials may be explained by migration of unbound compatibilizer from the surfaces of the PA microfibrils into a heterogeneous HDPE matrix (cf. Figure 13). This matrix is built both from well-developed semi-crystalline HDPE stacks that probe ε_n, and from a disordered fraction that has little effect on the long-period feature seen by the SAXS. The latter matrix fraction is characterized by almost random placement of diverse crystalline domains. If the migrating compatibilizer is enriched more in the disordered than in the ordered fraction, it can be expected that it plasticizes predominantly the fraction of the HDPE matrix in which it is enriched. Consequently, the nanoscopic strain in the disordered fraction would increase from cycle to cycle, whereas the probed ε_n would decrease slightly, as is observed in the experiments. In the literature similar softening effects of compatibilizers on the matrix of nanocomposites have been reported[43,44] and side-effects of additive migration in blends and composites have been studied[45–47]. By the way, migration of compatibilizer into the polyamide cannot be studied by means of SAXS data from the studied materials.

4.3.2 Response of the lateral nanoscopic strain

A different response scheme is observed with the lateral extensions $\varepsilon_{n,l}(t)$ of the crystallites. Figure 7 and Figure 8 present the data from the MFC precursors that contain PA6. Here, during the initial straining branch, $\varepsilon_{n,l}(t)$ is first increasing for small t showing domain-growth at low ε. We propose to explain this growth of the crystalline domains by strain-induced crystallization[48] ("epitaxial strain crystallization"). From higher ε and σ, the average $\varepsilon_{n,l}(t)$ begins to decrease. This indicates that now the dominant effect is domain destruction under high stress. For the MFC precursors containing PA12 the corresponding data are presented in Figure 9 and Figure 10. Here no epitaxial strain crystallization is observed.

The cycles of $\varepsilon(t)$ that follow the first straining induce oscillations of $\varepsilon_{n,l}(t)$. For the PA6-materials (Figure 7 and Figure 8) a phase shift is observed. The maxima of $\varepsilon_{n,l}(t)$ are always found on the increasing branch of $\varepsilon(t)$. Again, this finding is explained by epitaxial strain crystallization in the lower part of the branch followed by domain disruption in the upper part. The decreasing branch of $\varepsilon(t)$ is initially responded by further decrease of $\varepsilon_{n,l}(t)$ that can be explained by relaxation melting. In the lower part of the relaxation branch $\varepsilon_{n,l}(t)$ already starts to increase again. A possible reason is defragmentation of broken HDPE crystalline domains. For the PA12-materials, on the other hand, the phases of $\varepsilon(t)$ and $\varepsilon_{n,l}(t)$ are opposite (Figure 9 and Figure 10). Again, this finding coincides with the missing of epitaxial strain crystallization in the first straining branch of these materials. It is compatible with the notion of mere crystallite disruption in the straining branches, and in the relaxation branches of re-composition by defragmentation.

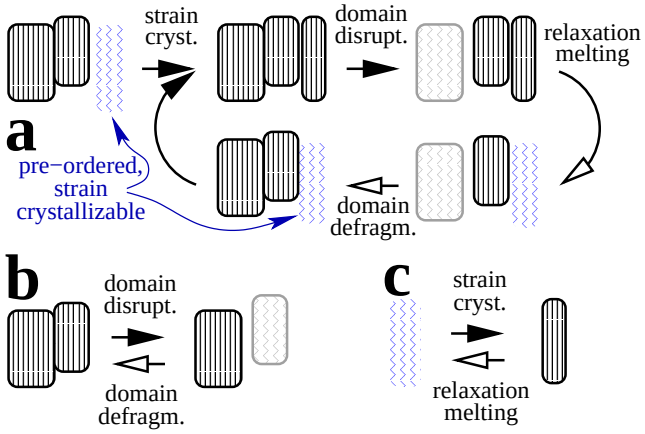

Figure 14: Schematic presentation of nanostructure evolution mechanisms during pre-straining and load-cycling. Only crystalline HDPE domains are depicted. Filled arrow-heads: Straining branches ($\dot{\varepsilon}(t) > 0$), open arrow-heads: relaxation branches ($\dot{\varepsilon}(t) < 0$). (**a**) Materials with PA6: The complex cycle includes epitaxial strain crystallization. (**b**) Materials with PA12: Simple cycle governed by domain disruption and domain defragmentation. (**c**) Speculative free strain crystallization for materials with PA12 from the evolution of the scattering power $Q(t)$

Figure 14 sketches the proposed nanostructure evolution mechanisms of the PA6-materials (Figure 14a) and of the PA12-materials (Figure 14b). The simpler scheme for PA12 can be explained by assuming that these materials do not contain enough pre-ordered amorphous HDPE chains around the crystalline HDPE domains to initiate significant domain growth by strain crystallization. Thus during the straining branches only continuous domain disruption and fragment dissolution is observed. During the relaxation branches the remnant pre-ordered amorphous regions from the fragments crystallize, and many of the original HDPE crystalline domains are reconstructed. Let us call this mechanism domain defragmentation. The PA6-materials, on the other hand, exhibit a more complex response to load-cycling that has also been found in a study[48] of pure polypropylene ((Figure 14a)). Here low stress suffices to extend and to crystallize pre-ordered HDPE chains that coat the crystalline domains. Higher stress disrupts HDPE crystalline domains and dissolves some of the fragments. Relaxation of some stress leads to melting of the strain-crystallized chains, and at very low stress fragments recombine.

The differences between low-pre-strain and high-pre-strain cycling is discussed by comparing the sub-figures a and b in Figure 7 – Figure 10, respectively. Obviously, the samples that are exposed to high pre-strain suffer higher damage to the nanostructure. This damage is not recovered during the following load-cycling.

4.3.3 Response of the scattering power

The variation of $Q(t)$ is only moderate. Together with the complex structure information contained in Q this makes interpretation highly speculative. The common initial response scheme of the scattering power $Q(t)$ is similar to that of $\varepsilon_{n,l}(t)$. During the first straining branch of $\varepsilon(t)$, $Q(t)$ passes through a maximum. According to Eq. (4) the interpretation of $Q(t)$ requires assumptions. Most probably the contrast does not change considerably, and the void scattering in the equatorial streak appears to be constant (cf. Figure 6). Moreover, if we assume that the initial volume crystallinity v is lower than 0.5, an increase of Q indicates increasing crystallinity. This daring assumption would fit well to the results of $\varepsilon_{n,l}(t)$ for the samples containing PA6. On the other hand, the initial volume crystallinity v_0 of HDPE is normally higher than 0.5, and in this case an increasing value of $Q \propto v(1-v)$ would indicate decreasing crystallinity.

Only if we would be willing to assume a small-angle volume-crystallinity $v_0 < 0.5$, the initial evolution of $Q(t)$ were indicative for strain crystallization in all materials. This would mean that strain crystallization would occur even in the PA12-blends, but here it would mainly induce the formation of new HDPE crystalline domains ("free strain crystallization"), and epitaxial strain crystallization were negligible. At least after several cycles $Q(t)$ responds by an oscillation that is in phase with the signal $\varepsilon(t)$. Under the low-crystallinity assumption this finding would, again, indicate free strain crystallization during the straining branch followed by melting during the relaxation branch (cf. Figure 14c).

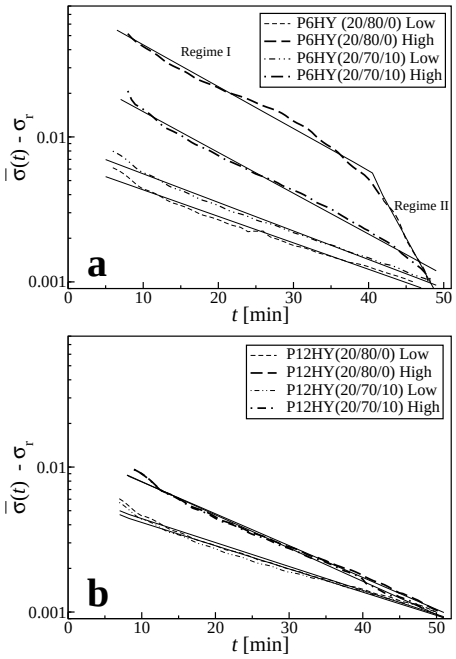

Figure 15: Assessment of fatigue by exponential regression of the macroscopic response $\bar{\sigma}(t)$. In order to linearize $\bar{\sigma}(t)$ a residual stress, σ_r, is subtracted. Here sufficient linearization has been obtained by setting $\sigma_r = \bar{\sigma}(t_{max})$. Solid straight lines illustrate the exponential fits to the data. **(a)** HDPE reinforced with PA6. **(b)** HDPE reinforced with PA12. The suffix **Low** indicates cycling about low pre-strain (ca. 5%) and **High** cycling about high pre-strain (ca. 8%). In high-cycling data of P6HY(20/80/0) two regimes are observed. Regime II is biased from sample bending after plastic flow

4.4 Plastic flow in P6HY(20/80/0)

Figure 7b shows the data from the load-cycling experiment about high pre-strain of P6HY(20/80/0). In the low-cycling test this material has shown considerable retardation of the nanostructure relaxation response (cf. Figure 12a). In the high-cycling test after 40 min the ε returns negative values. This result is an artifact because the sample bends, whereas the distances between the fiducial marks are still measured along the fixed straight axis of the ROI. The bending is clearly observed in the video frames and demonstrates macroscopic plastic flow. Plastic flow is also indicated by the strong decrease of $\sigma(t)$. Moreover, this experiment is the only one that returns decreasing ε_n values. Thus the average distance between the crystallites from the nanofibrils (ordered stacks) is shrinking while the material is lengthened on the macroscopic scale. This combination of plastic flow and long-period shrinkage can be explained by disentanglement of the HDPE chains outside the nanofibrils that leads to macroscopic plastic flow and eliminates frozen-in tension on the nanoscopic scale.

4.5 Material fatigue

In common fatigue tests the macroscopic stress $\sigma(t)$ is controlled, and the strain $\varepsilon(t)$ is the macroscopic response. Because of the limited capabilities of our tensile tester we have controlled $\varepsilon(t)$. Thus $\sigma(t)$ is the macroscopic response, and macroscopic fatigue of the materials is indicated by the decay of the peak stresses from cycle to cycle. For a quantitative analysis it appears reasonable to level out the oscillations of $\sigma(t)$ by computing the running average $\bar{\sigma}(t)$ over one period of the signal $\varepsilon(t)$.Figure 15 shows the variation of $\bar{\sigma}(t)$in a semi-logarithmic plot together with lines that indicate an exponential regression using the equation $y = k\exp(-t/\tau)$. Here k and τ are the regression parameters with τ the lifetime of the decay. Lower lifetimes correspond to stronger fatigue.

Table 3 reports extreme values of the mechanical parameters and the lifetimes τ determined from the load-cycling data. ε_{max} is the maximum strain, σ_{max} the maximum stress that is reached in the 1st maximum of load cycling, and σ_2/σ_{max} is the ratio of the 2nd to the 1st stress maximum. This

value is included in the table because for $t < 10$ min the decay of $\bar{\sigma}(t) - \sigma_r$ is faster than the fitted exponential. Thus σ_2/σ_{max} is a better measure for the initial fast stress decay. Higher values of σ_2/σ_{max} mean less stress fatigue. The table shows that fatigue is higher when the sample is cycled about higher pre-strain. Fatigue is lower in the blends reinforced by PA12 than in the samples containing PA6. The low fatigue of PA12-materials may be explained by higher compatibility with HDPE due to the longer aliphatic chain segments of PA12. A practical explanation of the lower fatigue is the less-deteriorated semi-crystalline nanostructure of the HDPE in the PA12-materials (Figure 5). Apparently, addition of 10 wt.-% compatibilizer does not reduce the material fatigue significantly. This may be related to the finding that addition of the compatibilizer leads to strain heterogenization during load cycling (cf. Figure 12).

Table 3: Slow load cycling of MFC precursor materials. Extreme mechanical parameters and lifetime τ of stress fatigue. "Low" indicates cycling about $\varepsilon \approx 0.05$, "High" about $\varepsilon \approx 0.08$. σ_2/σ_{max} is the ratio of the 2nd to the 1st stress maximum

sample code	ε_{max}	σ_{max} [MPa]	σ_2/σ_{max}	τ [min]
P6HY(20/80/0) Low	0.058	62	0.96	24
P6HY(20/80/0) High	0.095	98	0.80	15
P6HY(20/70/10) Low	0.054	72	0.93	22
P6HY(20/70/10) High	0.081	137	0.91	15
P12HY(20/80/0) Low	0.054	64	0.95	26
P12HY(20/80/0) High	0.091	89	0.93	20
P12HY(20/70/10) Low	0.058	64	0.94	28
P12HY(20/70/10) High	0.094	100	0.93	19

5 Conclusions

After having performed this study we have learned that

1. Monitoring of practical fatigue tests of anisotropic polymer materials by quantitative SAXS will require further development of technique at synchrotron radiation facilities. Exposure is still too long.

2. The observed heterogeneous strain distribution in the material may, ultimately, deteriorate the performance of the composite. This result indicates the complexity of composite design, because the desired effects of an additive or a processing step may be accompanied by side effects[43–47].

3. In-situ monitoring of structure evolution under simulated service conditions may advance the awareness of important parameters and, finally, accelerate the design by guiding the focus of the designer. For example concerning compatibilization, one would not only vary the compatibilizer fraction, but also the mixing procedure (e.g. premixing[33,34]), the block lengths of the compatibilizer, and the temperature profile of the processing. At the optimum the mixing and the initial temperature profile should result in a constant average compatibilizer density in the interfacial layer, sufficient block lengths should restrict further compatibilizer motion away from the interfacial layer during service, and sufficiently short blocks should keep the mobility of the compatibilizer high enough to guarantee its homogeneous distribution in the interface, until it is finally locked immobilized either by chemical reaction or by quenching.

4. For the studied MFC precursors the final step of matrix isotropization has not yet been carried out. This step is performed at high temperature and pressure, i.e. at conditions that promote additional chemical and physical interactions. Therefore, some of the results found with the precursors might not be fully valid for the final MFC materials.

5. A heterogeneous strain distribution is not only indicated by $\varepsilon_n/\varepsilon < 1$, but also by $\varepsilon_n/\varepsilon > 1$. In the last-mentioned case the well-developed semi-crystalline stacks would respond with a higher strain (ε_n) than the macroscopic average (ε), showing that under load the heavily disordered or amorphous fraction of the matrix polymer would yield less than the macroscopic average.

Acknowledgements: The authors thank the Hamburg Synchrotron Radiation Laboratory (HASYLAB) for beam time granted in the frame of projects II-2008-0015 and I-2011-0087. This work has been partially supported by the 7th framework program of the European Union (Project NANOTOUGH FP7-NMP-2007-LARGE). One of us (ND) gratefully acknowledges the financial support by the Portuguese *Fundação para a Ciência e Tecnologia* under the grant SFRH/BPD/45252/2008.

Manuscript version submitted to the publisher that contains the original color graphics.

Keywords: compatibilization; composites; fatigue analysis; SAXS; structure-property relations

References

[1] S. Fakirov, M. Evstatiev, *Adv. Mater.* **1994**, *6*, 395.
[2] S. Fakirov, M. Evstatiev, K. Friedrich, in: D. R. Paul, C. D. Bucknall, Eds. "Polymer Blends", J. Wiley & Sons, New York, vol. 2, **2000** p. 455.
[3] B. Alcock, N. O. Cabrera, N.-M. Barkoula, C. T. Reynolds, L. E. Govaert, T. Peijs, *Compos. Sci. Techn.* **2007**, *67*, 2061.
[4] C. Roy, A. Chaala, *Resources, Conservation and Recycling* **2001**, *32*, 1.

[5] M. Day, Z. Shen, J. D. Cooney, *J. Anal. Appl. Pyrolysis* **1999**, *51*, 181.
[6] F. E. Mark, M. Fisher, M., K. A. Smith, in: F. E. Mark, M. M. Fisher, K. A. Smith, Eds. "Energy Recovery from automotive shredder residue", Assoc. Plastics Manufacturers in Europe (APME), Brussels, **1998** pp. 158–175.
[7] M. Evstatiev, S. Fakirov, *Polymer* **1992**, *33*, 877.
[8] Z. Z. Denchev, N. V. Dencheva, *Polym. Inter.* **2008**, *57*, 11.
[9] D. Thorby, *Structural Dynamics and Vibration in Practice*, Butterworth-Heinemann, Amsterdam, 1st edition, **2008**.
[10] A. Peterlin, *Ann. Rev. Mater. Sci.* **1972**, *2*, 349.
[11] M. T. Takemori, *Ann. Rev. Mater. Sci.* **1984**, *14*, 171.
[12] B. Crist, *Ann. Rev. Mater. Sci.* **1995**, *25*, 295.
[13] A. Pegoretti, in: J. Karger-Kocsis, S. Fakirov, Eds. "Nano- and Micro-Mechanics of Polymer Blends and Composites", Hanser, Munich, **2009** pp. 301–339.
[14] N. Stribeck, in: J. Karger-Kocsis, S. Fakirov, Eds. "Nano- and Micromechanics of Polymer Blends and Composites", Hanser Publisher, Munich, vol. 1, **2009** pp. 269–300.
[15] N. Stribeck, *J. Macromol. Sci. Part C: Polymer Reviews* **2010**, *50*, 40.
[16] H. R. Brown, E. J. Kramer, R. A. Bubeck, *J. Mater. Sci.* **1988**, *23*, 248.
[17] H. R. Brown, E. J. Kramer, R. A. Bubeck, *J. Polym. Sci. Part B: Polym. Phys.* **1987**, *25*, 1765.
[18] S. Toki, I. Sics, C. Burger, D. Fang, L. Liu, B. S. Hsiao, S. Datta, A. H. Tsou, *Macromolecules* **2006**, *39*, 3588.
[19] N. Dencheva, Z. Denchev, M. J. Oliveira, S. S. Funari, *Macromolecules* **2010**, *43*, 4617.
[20] N. Dencheva, M. J. Oliveira, O. S. Carneiro, A. S. Pouzada, Z. Denchev, *J. Appl. Polym. Sci.* **2010**, *115*, 2918.
[21] S. Ran, X. Zong, D. Fang, B. S. Hsiao, B. Chu, R. Ross, *J. Appl. Cryst.* **2000**, *33*, 1031.
[22] N. Stribeck, U. Nöchel, S. S. Funari, T. Schubert, *J. Polym. Sci. Polym. Phys.* **2008**, *46*, 721.
[23] Z. Denchev, N. Dencheva, S. S. Funari, M. Motovilin, T. Schubert, N. Stribeck, *J. Polym. Sci. Part B: Polym. Phys.* **2010**, *48*, 237.
[24] N. Stribeck, *X-Ray Scattering of Soft Matter*, Springer, Heidelberg, New York, **2007**.
[25] N. Stribeck, U. Nöchel, *J. Appl. Cryst.* **2008**, *41*, 715.
[26] N. Stribeck, *J. Appl. Cryst.* **2001**, *34*, 496.
[27] S. Ran, X. Zong, D. Fang, B. S. Hsiao, B. Chu, R. A. Phillips, *Macromolecules* **2001**, *34*, 2569.
[28] A. Jánosi, *Monatsh. f. Chemie* **1983**, *114*, 377.
[29] O. Glatter, O. Kratky, Eds. *Small Angle X-ray Scattering*, Academic Press, London, **1982**.
[30] F. J. Baltá Calleja, C. G. Vonk, *X-Ray Scattering of Synthetic Polymers*, Elsevier, Amsterdam, **1989**.
[31] N. Stribeck, A. Zeinolebadi, M. Ganjaee Sari, A. Frick, M. Mikoszeg, S. Botta, *Macromol. Chem. Phys.* **2011**, *212*, 2234.
[32] N. V. Dencheva, M. J. Oliveira, A. S. Pouzada, M. P. Kearns, Z. Z. Denchev, *Polymer Composites* **2011**, *32*, 407.
[33] M. Krumova, G. H. Michler, M. Evstatiev, K. Friedrich, S. Fakirov, in: "Proc. of PC2003: Polymer Crystallization, Linz, Austria", **2003** .
[34] M. Krumova, G. Michler, M. Evstatiev, K. Friedrich, N. Stribeck, S. Fakirov, *Progr. Colloid Polym. Sci.* **2005**, *130*, 167.
[35] A. Peterlin, *Text. Res. J.* **1972**, *42*, 20.
[36] G. Porod, *Fortschr. Hochpolym.-Forsch.* **1961**, *2*, 363.
[37] W. O. Statton, *J. Polym. Sci.* **1962**, *58*, 205.
[38] S. Kumar, S. Warner, D. T. Grubb, W. W. Adams, *Polymer* **1994**, *35*, 5408.
[39] S. Fakirov, O. Samokovlijsky, N. Stribeck, A. A. Apostolov, Z. Denchev, D. Sapoundjieva, M. Evstatiev, A. Meyer, M. Stamm, *Macromolecules* **2001**, *34*, 3314.
[40] R. Androsch, N. Stribeck, T. Lüpke, S. Funari, *J. Polym. Sci. Part B: Polym. Phys.* **2002**, *40*, 1919.
[41] S. Humbert, O. Lame, J.-M. Chenal, C. Rochas, G. Vigier, *J. Polym. Sci. Part B: Polym. Phys.* **2010**, *48*, 1535.
[42] J. A. H. W. Moonen, W. A. C. Roovers, R. J. Meier, B. J. Kip, *J. Polym. Sci. Part B: Polym. Phys.* **1992**, *30*, 361.
[43] J. Fröhlich, R. Thomann, R. Mühlhaupt, *Macromolecules* **2003**, *36*, 7205.
[44] A. M. Díez-Pascual, Naffakh, Mohammed, J. González-Domínguez, A. Ansón, Y. Martínez-Rubi, M. T. Martínez, B. Simard, M. A. Gómez, *Carbon* **2010**, *48*, 3500.
[45] E. Földes, *Angew. Makromol. Chem.* **1998**, *261-265*, 65.
[46] H. E. Burch, C. E. Scott, *Polymer* **2001**, *42*, 7313.
[47] V. Thirtha, R. Lehman, T. Nosker, *J. Appl. Polym. Sci.* **2008**, *107*, 3987.
[48] N. Stribeck, U. Nöchel, S. S. Funari, T. Schubert, A. Timmann, *Macromol. Chem. Phys.* **2008**, *209*, 1992.

For the Table of Contents:

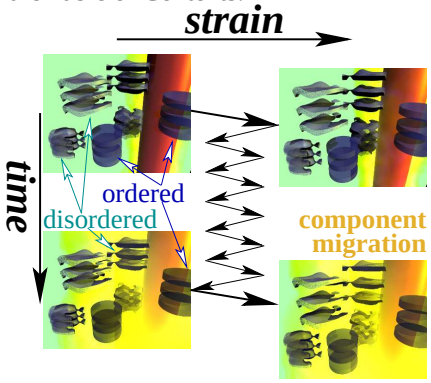

Composite design is a complex task, because the desired effects of a component or a processing step may be accompanied by side effects. Monitoring the nanostructure under service conditions may accelerate the design by guiding the focus of the designer.